

# Temperature Measurement of Quark-Gluon Plasma at Different Stages

STAR Collaboration

In a Quark-Gluon Plasma (QGP), the fundamental building blocks of matter, quarks and gluons, are under extreme conditions of temperature and density <sup>1-4</sup>. A QGP could exist in the early stages of the Universe <sup>5-7</sup>, and in various objects and events in the cosmos <sup>8-10</sup>. The thermodynamic and hydrodynamic properties of the QGP are described by Quantum Chromodynamics (QCD) and can be studied in heavy-ion collisions <sup>11,12</sup>. Despite being a key thermodynamic parameter, the QGP temperature is still poorly known. Thermal lepton pairs ( $e^+e^-$  and  $\mu^+\mu^-$ ) are ideal penetrating probes of the true temperature of the emitting source, since their invariant-mass spectra suffer neither from strong final-state interactions nor from blue-shift effects due to rapid expansion <sup>13-15</sup>. Here we measure the QGP temperature using thermal  $e^+e^-$  production at the Relativistic Heavy Ion Collider (RHIC). The average temperature from the low-mass region (in-medium  $\rho^0$  vector-meson dominant) is  $(1.99 \pm 0.24) \times 10^{12}$  K, consistent with the chemical freeze-out temperature from statistical models <sup>16</sup> and the phase transition temperature from LQCD <sup>17,18</sup>. The average temperature from the intermediate mass region (above the  $\rho^0$  mass, QGP dominant) is significantly higher at  $(3.40 \pm 0.55) \times 10^{12}$  K. This work provides essential experimental thermodynamic measurements to map out the QCD phase diagram and understand the properties of matter under extreme conditions.

## 1 Introduction

The state of QCD matter is typically characterized by its temperature and baryon chemical potential, as depicted in Fig. 1. In standard thermodynamics, the baryon chemical potential,  $\mu_B$ , is a measure of the change in free energy due to an increase of baryon number by one in a fixed volume, and increases monotonically with net baryon density. Dielectrons, i.e., electron-positron pairs, are excellent thermometers of the extremely hot and dense QCD matter<sup>1,19–21</sup> created in high-energy heavy-ion collisions. All leptons do not participate directly in the strong interactions; consequently electrons and positrons have minimal interactions with the predominantly strongly-interacting particles throughout the evolution of the system in both its initial quark-gluon and its final hadronic states. As is the case for any black-body radiation spectrum, higher temperatures yield harder dielectron energy and mass spectra, i.e., exhibit an increase in the ratio of high to low mass pairs<sup>13,14</sup>. QGP consists of locally thermalized quarks and gluons with temperatures in excess of hundreds of MeV (where 100 MeV corresponds to  $1.16 \times 10^{12}$  K), higher than the QCD critical temperature ( $T_C$ ). Theoretical studies<sup>17</sup> from lattice QCD (LQCD) predict a crossover transition with a smooth but rapid change of thermodynamic quantities in a narrow region around  $T_C \sim 156.5$  MeV at  $\mu_B < 300$  MeV. Following the initial stage of a heavy-ion collision, the system cools down as it expands rapidly. Throughout its expansion, the hot system radiates both photons and lepton pairs which can be measured by dedicated particle detectors. As a result, different ranges of the dielectron energy and mass spectra are dominated by the radiation at the different stages of the system's evolution. Photon momentum spectra have been used to determine the QGP temperature at the Relativistic Heavy Ion Collider (RHIC) and the Large Hadron Collider (LHC) during the past two

decades<sup>22–25</sup>. However, an unambiguous interpretation is complicated by the rapid bulk expansion at those collision energies because the expansion velocity is a substantial fraction of the speed of light and it alters the energy spectrum of the photons. This blue-shift effect makes it very difficult, if not impossible, to extract the true “blackbody” radiation temperature from the detected photon energy spectrum and overly reliant on model assumptions<sup>15</sup>. On the other hand, electron-positron pairs from thermal emissions provide an additional degree of freedom through the reconstruction of their invariant mass,  $M_{ee}$ , a frame-independent variable<sup>13,14</sup>. The invariant-mass spectrum of thermal dielectrons is immune to blue-shift effects and is thus able to provide a true measurement of the temperature of the QGP at different stages of the evolution. In the early stage of QGP evolution, thermal dielectrons are predominantly produced via the annihilation processes among quarks and anti-quarks. During the phase transition, as the system cools down, deconfined quarks begin to hadronize into colorless baryons and mesons. The resulting strongly-interacting mixed medium, with both partonic and hadronic degrees of freedom, still exhibits bulk thermodynamic and hydrodynamic properties and continues to expand and cool down. At this stage and later on, dielectrons primarily arise from the decay of  $\rho^0(770)$  vector mesons produced inside the medium. The dense hadronic medium continuously creates  $\rho^0$  mesons through frequent hadronic interactions. The  $\rho^0$  meson with a lifetime of about  $1.3 \text{ fm}/c$  mostly decays inside the medium that lasts for teens of  $\text{fm}/c$ <sup>15</sup>. Consequently, the invariant-mass spectrum of the in-medium  $\rho^0$  reconstructed via dielectrons is considered an excellent experimental probe of the dissolving hadronic mass line-shape close to the QCD phase transition<sup>26–29</sup>. In the subsequent evolution, the system experiences a stage in which the inelastic interactions among particles cease due to decreasing density, resulting

in the freezing of particle composition. This stage is known as the chemical freeze-out<sup>16</sup>. Elastic interactions continue after freeze-out, and these influence particle momenta. At the very last stage of the expansion, elastic interactions stop, and the system enters the stage of kinetic freeze-out<sup>30</sup>.

During the past three decades, measurements of the thermal dilepton ( $e^+e^-$  and  $\mu^+\mu^-$ ) production in heavy-ion collisions over a wide range of collision energies have been an essential scientific program of several experiments conducted at particle accelerator facilities such as the Bevalac<sup>31</sup>, the SIS18<sup>32</sup>, the SPS<sup>33–35</sup>, RHIC<sup>36–40</sup>, and the LHC<sup>41</sup>. The measured dilepton spectra in the low-mass region from SPS to RHIC energies have provided strong experimental evidence that the spectral function of the in-medium  $\rho^0$  vector meson is substantially broadened without significant change of its mass peak<sup>26–29</sup>. Furthermore, the effective temperature  $T_{\text{eff}}$ , an inverse slope parameter of the dimuon transverse-mass spectra, was extracted from NA60 data in In+In collisions at nucleon-nucleon center-of-mass energy  $\sqrt{s_{\text{NN}}} = 17.3 \text{ GeV}$ <sup>35</sup>. This  $T_{\text{eff}}$  has been observed to increase linearly as a function of the dimuon invariant mass up to  $M_{\mu\mu} < 1 \text{ GeV}/c^2$ , followed by a decrease at higher masses. This feature is consistent with the expectation that the momenta of the low-mass dimuons from hadronic decays, including the in-medium  $\rho^0$ , are shifted toward higher momenta when emitted from a hadronic medium with a large collective radial flow. Higher mass thermal dimuons, on the other hand, are predominantly produced in a partonic medium at an earlier stage of the collision with much less radial flow. The HADES experiment has recently shown that the dielectron mass spectrum exhibit a near-exponential fall-off in the low-mass region in Au+Au collisions at  $\sqrt{s_{\text{NN}}} = 2.42 \text{ GeV}$ <sup>32</sup>. The average temperature extracted from this exponential spectrum was determined to be  $71.8 \pm 2.1 \text{ MeV}$ . Although its kinematic reach is below the  $\rho^0$  pole

mass ( $775 \text{ MeV}/c^2$ ), the result indicates that the  $\rho^0$  resonance spectrum is significantly altered by the frequent interactions among the baryons in the dense hadronic medium and the process could produce a seemingly thermalized system. Such measurements and knowledge at lower beam energies provide the necessary baseline for temperature measurements at different stages of collisions at higher energies. In this article, we present dielectron spectra in Au+Au collisions at  $\sqrt{s_{\text{NN}}} = 27$  and 54.4 GeV using experimental data from the STAR detector at RHIC, collected in years 2017 and 2018. The temperatures of hot nuclear matter in the low-mass and intermediate-mass regions are extracted from the thermal dielectron distributions. These results provide unique access to the thermodynamic properties at both the early stage of the QGP phase, and the late stage near the phase transition to hadronic matter.

## 2 Experiment

The most relevant subdetectors of the STAR detector are depicted in Fig. 2 (top panel) together with a typical event display from a heavy-ion collision. Charged particles produced in these collisions leave ionization trails inside the Time Projection Chamber (TPC) <sup>42</sup>. The radius of curvature of a charged particle trajectory in an externally applied magnetic field ( $B = 0.5 \text{ Tesla}$ ) is used to determine its momentum per charge ( $p/q$ ). The ionization energy loss per unit length ( $dE/dx$ ) along a particle's path through the TPC gas as a function of its  $p/q$  is shown in Fig. 2. Combining the time-of-flight information measured by TOF with the path length and momentum information, the mass ( $m$ ) of charged particles can be obtained. The electrons of interest have the typical characteristics of a relativistic rise in  $dE/dx$  and low  $m^2$  as shown in Fig. 2. These two pow-

erful particle identification techniques provide high-purity electron identification with a hadronic background rejection rate of more than 5 orders of magnitude and a large fiducial acceptance<sup>38,43</sup>. The identified electrons and positrons from the same event are combined to reconstruct the invariant mass and transverse momentum of all possible pairs. However, more than 99% of these pairs are random combinations, commonly referred to as the combinatorial background, which need to be subtracted in order to obtain the inclusive dielectron signals<sup>38</sup>. Following corrections for the pair reconstruction efficiency and acceptance, the fully corrected inclusive dielectron signal is established as shown in the top two panels of Fig. 3. More details on these and other analysis procedures can be found in the Methods Section.

The measured inclusive dielectron spectra are an accumulation of contributions from various stages throughout the evolution of the system following a heavy-ion collision. These include dielectrons from the thermal QCD medium of the collision and also from non-thermal physical sources. At the very early stages, dielectrons are produced through the Drell-Yan processes<sup>44</sup> in which quarks and anti-quarks from the colliding nucleons annihilate through virtual photons into lepton pairs. At much later stages, after the hot medium has disintegrated, dielectrons are produced from the decays of (relatively) long-lived hadrons. These include the two-body decays from  $\omega$ ,  $\phi$ ,  $J/\psi \rightarrow e^+e^-$ , Dalitz decays<sup>45</sup> from  $\pi^0$ ,  $\eta$ ,  $\eta'$ ,  $J/\psi \rightarrow \gamma e^+e^-$  and  $\omega \rightarrow \pi^0 e^+e^-$ ,  $\phi \rightarrow \eta e^+e^-$ , and the weak, semi-leptonic decays of open-charm hadrons. The contributions from these physics backgrounds are commonly referred to as the “cocktail” and can be well determined from simulations, shown in the top two panels of Fig. 3. The fully corrected data substantially exceed the total physical background “Cocktail Sum” over a large mass region due to significant contributions from

thermal dielectrons and the  $\rho^0$  meson at lower masses. To quantify the thermal component, the excess dielectron mass spectrum is obtained by subtracting the cocktail sum from the measured, fully corrected inclusive data. Further details about the cocktail simulations can be found in the Methods Section.

### 3 Results and Discussions

The measured invariant-mass spectra of the thermal dielectrons (i.e., the excess dielectrons) are shown in the bottom panel of Fig. 3. The spectra are normalized by the charged particle multiplicity at mid-rapidity  $dN_{\text{ch}}/dy|_{y=0}$  in order to compare the measurements among different colliding species and beam energies. Two important invariant-mass ranges in this study are defined as follows: the low-mass region (LMR),  $0.4 < M_{ee} < 1.20 \text{ GeV}/c^2$ , and the intermediate-mass region (IMR),  $1.0 < M_{ee} < 2.9 \text{ GeV}/c^2$ . The bottom panel of Fig. 3 shows the LMR results where the STAR Au+Au collision data at  $\sqrt{s_{\text{NN}}} = 27$  and  $54.4 \text{ GeV}$  are consistent with each other within the entire mass region. The STAR LMR data also show good agreement with the dimuon results from In+In collisions at  $\sqrt{s_{\text{NN}}} = 17.3 \text{ GeV}$ , while the Au+Au IMR data are systematically higher than the NA60 data. These observations suggest that in the LMR, the thermal dileptons from the three measurements originate from radiative sources with a similar temperature, while the thermal dileptons in the IMR originate from sources with different temperatures. To quantify the temperature of the thermal source responsible for LMR radiation, a function that combines the in-medium resonance structure and the continuum thermal distribution is used to fit the measured mass spectrum. The mass lineshape of  $\rho^0$  decaying to dileptons in vacuum can be described by a relativistic

Breit-Wigner function <sup>46-48</sup>,  $f^{\text{BW}}(M) = \frac{MM_0\Gamma}{(M_0^2 - M^2)^2 + M_0^2\Gamma^2}$ , where  $M$  is the invariant mass of the dilepton pair and  $\Gamma = \Gamma_0 \frac{M_0}{M} \sqrt{\frac{M^2 - 4m^2}{M_0^2 - 4m^2}}$  is the width.  $M_0$  and  $\Gamma_0$  are the pole mass and width of  $\rho^0$  meson, while  $m$  is the lepton mass. When presented inside a hot QCD medium, the  $\rho^0$  mass lineshape can be described by  $f^{\text{BW}}(M)$ , multiplied by the Boltzmann factor  $e^{-M/k_{\text{B}}T}$  to account for the phase space <sup>49,50</sup>. Both  $f^{\text{BW}}(M)$  and the Boltzmann factor are highly dependent on the medium temperature. If the  $\rho^0$  is completely dissolved in the medium, its mass spectral structure ( $f^{\text{BW}}(M)$ ) spreads out and approaches a smooth distribution similar to a  $q\bar{q}$  continuum (QGP thermal radiation) <sup>14,32</sup> which can be described by  $M^{3/2}e^{-M/k_{\text{B}}T}$ . The extracted temperatures  $T_{\text{LMR}}$  from the LMR thermal dielectron mass spectra are  $167 \pm 21$  (stat.)  $\pm 18$  (syst.) MeV and  $172 \pm 13$  (stat.)  $\pm 18$  (syst.) MeV for the Au+Au collisions at  $\sqrt{s_{\text{NN}}} = 27$  and 54.4 GeV, respectively. A similar fit to the NA60 data (shown in the Methods Section) gives a temperature of  $165 \pm 4$  MeV. The temperatures extracted from the LMR thermal dileptons of different collision energies and species are consistent with each other and in agreement with the conjecture (discussed in the previous section) that they are radiated from thermal sources with a similar temperature. The IMR results for the 27 GeV and 54.4 GeV Au+Au collisions are also consistent within their uncertainties. The mass spectrum in this mass region is smooth, and the temperature is extracted by fitting the Boltzmann function  $M^{3/2}e^{-M/k_{\text{B}}T}$  <sup>14</sup>. The extracted temperatures  $T_{\text{IMR}}$  for the 27 GeV and 54.4 GeV Au+Au collisions are  $280 \pm 64$  (stat.)  $\pm 10$  (syst.) MeV and  $303 \pm 59$  (stat.)  $\pm 28$  (syst.) MeV, respectively. By fitting the thermal dimuon spectra of In+In data in this mass region (shown in the Methods Section), a temperature of  $245 \pm 17$  MeV is extracted. For all the systems, the extracted temperature for the low-mass range is significantly lower than that of the intermediate-



mass range. This observation is consistent with the expectation that LMR thermal dileptons are predominantly emitted at a later stage of the medium evolution around the phase transition, while those in the IMR are mainly from the earlier partonic stage with much higher temperatures. It should be noted that these temperature values from the IMR are systematically higher than model estimations using entropy and adiabatic thermodynamic expansions<sup>14</sup>. Radiation at an early stage, when the system is in a non-equilibrium state, may contribute to the IMR dielectrons and yield a higher apparent temperature<sup>51</sup>. Future experimental data with high statistics and further model studies are necessary.

Figure 4 summarizes the temperature measurements as a function of the baryon chemical potential  $\mu_B$ . The chemical freeze-out temperature  $T_{\text{ch}}$  and  $\mu_B$  can be well determined by applying statistical thermal models<sup>16</sup> to the hadron production yields. The chemical freeze-out temperatures extracted from various statistical thermal models (SH, GCE, SCE)<sup>16,52</sup> are shown in the figure as filled and open circles. Similarly, temperatures were extracted from previously published low-mass thermal dielectron spectra<sup>37,39</sup> with a thermal distribution of  $M^{3/2}e^{-M/k_B T}$ . The extracted  $T_{\text{LMR}}$  from the limited statistics of those measurements are in good agreement with STAR's new results from Au+Au collisions at  $\sqrt{s_{\text{NN}}} = 27$  and 54.4 GeV as well as the result extracted from NA60 In+In data at  $\sqrt{s_{\text{NN}}} = 17.3$  GeV. Moreover, all these  $T_{\text{LMR}}$  values are found to be consistent with  $T_C$  and  $T_{\text{ch}}$ .

A long-standing challenge has been the empirical observation that the  $T_{\text{ch}}$  extracted from the yields of the final-state hadrons coincides with the QCD phase transition temperature ( $T_C$ ) from

LQCD <sup>16</sup>. Stable hadrons emerge from the chemical freeze-out and their yields are an integration over the whole volume of the system. Therefore, the extracted  $T_{\text{ch}}$  by definition should have been lower than the phase transition temperature. The present dilepton measurements can provide new insight towards resolving this puzzle. The measured yields of the low-mass thermal dileptons are an accumulation from the initial QGP stage to the final kinetic freeze-out. Therefore, these yields are integrated over the whole system volume and over the entire radiative evolution time. These measured dilepton yields can be compared to those from  $\rho^0$  decays in the vacuum at chemical freeze-out estimated from the two baseline measurements of the  $\rho^0$  yields from its  $\pi^+\pi^-$  decay channel in proton-proton and  $e^+e^-$  collisions. A comparison of the charged-particle multiplicity ( $dN_{\text{ch}}/dy|_{y=0}$ ) normalized dilepton yields measured in heavy-ion collisions with the expected dilepton yields at freeze-out clearly shows that the measured dielectron yields (within  $0.4 - 0.75$  GeV/ $c^2$  mass window) are more than a factor of 5 larger than those two baseline yields (cf. Fig. 3 bottom panel and Methods Section). The high yields of dileptons, the strong in-medium broadening of the  $\rho$  spectral function, and the approximate overlap of  $T_C$ ,  $T_{\text{ch}}$  and  $T_{\text{LMR}}$  at these energies suggest that the low-mass thermal dileptons are predominantly emitted over a long period of time at high density around a fixed temperature. Such a scenario is possible under the assumption of strong influence by a phase transition <sup>14,53</sup> and/or by a soft point in the equation of state <sup>54,55</sup>. These measurements provide a direct experimental tool for accessing the temperature in the vicinity where the phase transition to deconfinement occurs - one of the most fundamental landmarks of the QCD phase diagram.

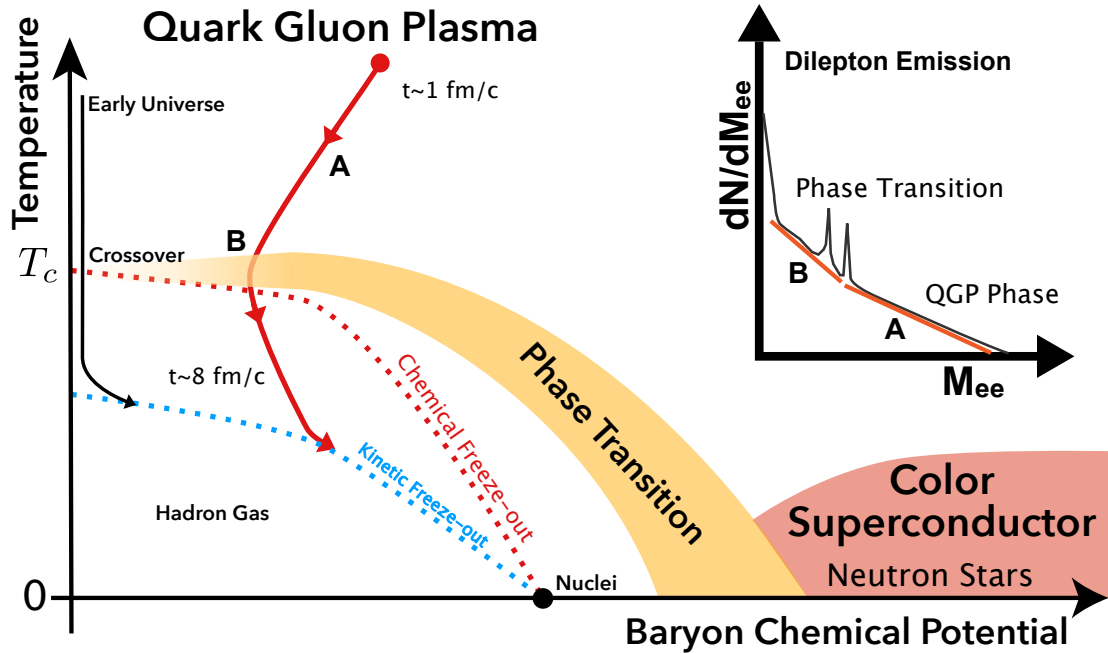


Figure 1: A schematic view of  $e^+e^-$  pair production and the QCD phase diagram. The diagram illustrates matter properties with baryon chemical potential (equivalent to net baryon number density) and temperature, with landmarks of normal nuclei, neutron stars, and the phase transition to QGP. A heavy-ion collision creates a QGP at high baryon chemical potential and high temperature shortly after the initial impact, and the system evolves along the red arrow toward the phase boundary and hadronization. The insert depicts the dilepton spectrum with low-mass and intermediate-mass ranges corresponding to the dominant emission contribution from the transition and the QGP phases, respectively.

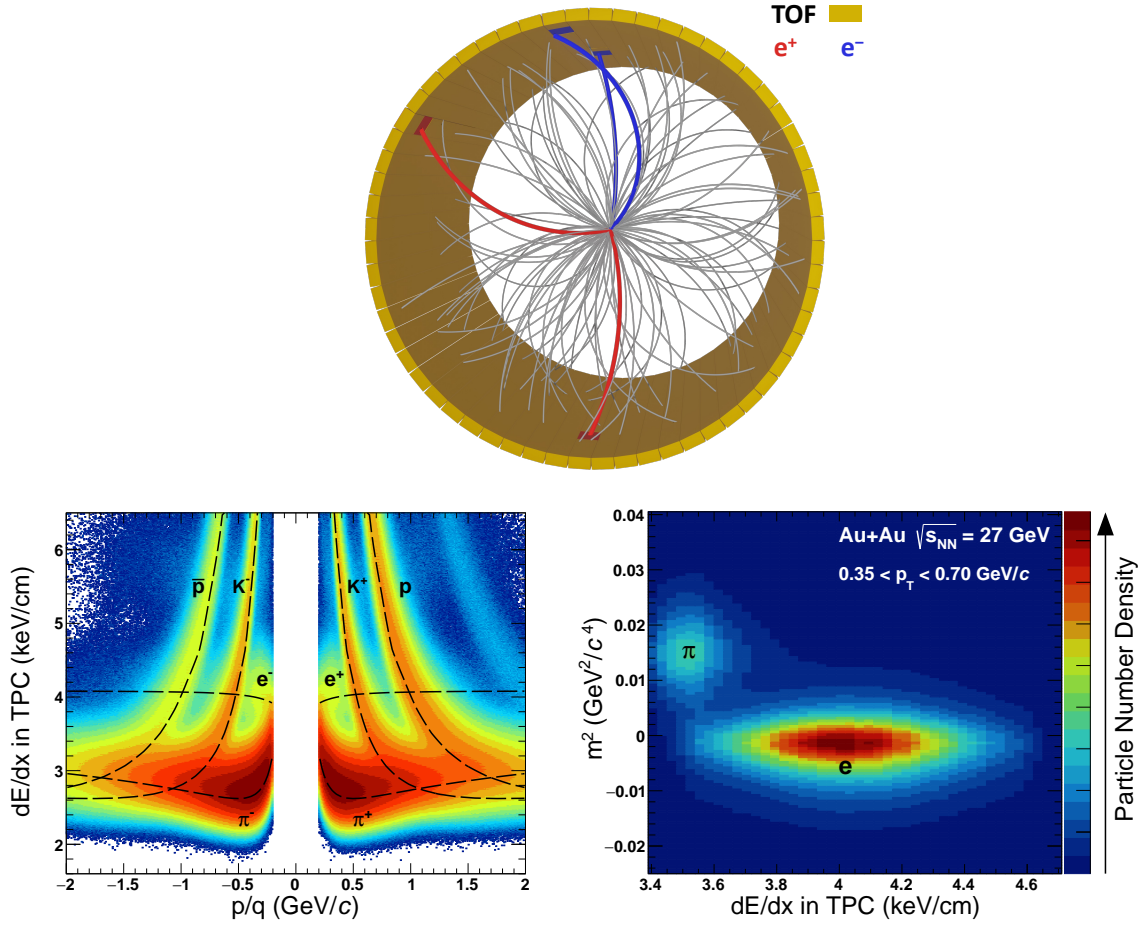


Figure 2: A schematic display of a Au+Au collision reconstructed with the STAR detector. The top panel shows charged-particle ionization in the gas of the STAR TPC, forming three-dimensional tracks (gray lines) that curve due to the magnetic field of the detector. As tracks exit the outer radius of the TPC, they leave signals (red and blue hits) in the TOF detector. Electrons (blue tracks) and positrons (red tracks) tracks are identified based on the ionization energy loss  $dE/dx$  and mass squared  $m^2$  measured by the TPC and TOF. The bottom-left panel shows the  $dE/dx$  as a function of momentum per charge  $p/q$ , and the bottom-right panel shows the  $m^2$  vs.  $dE/dx$  distribution of the electron candidates.

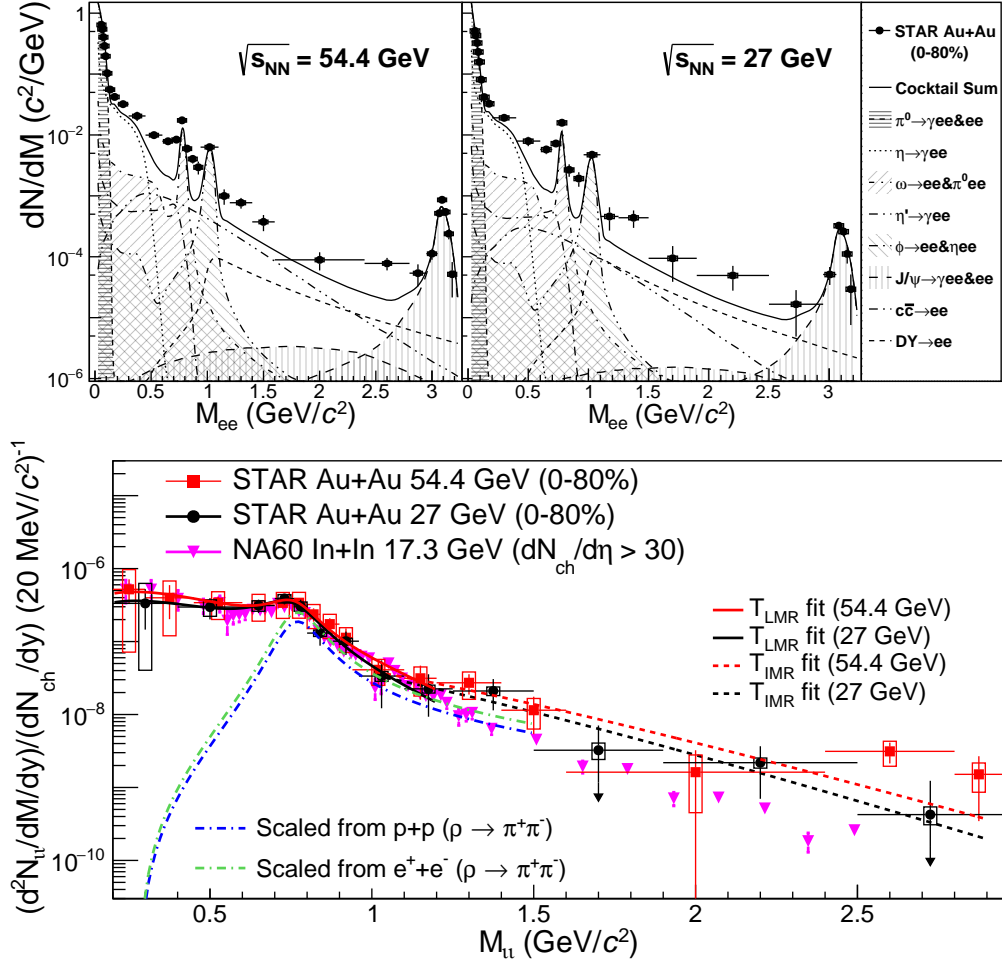


Figure 3: **Dielectron invariant-mass spectra.** The top panel shows the fully corrected inclusive dielectron mass spectra (black dots) compared to the physics background (dashed lines and shaded lines) in Au+Au minimum-bias (0-80% centrality) collisions at  $\sqrt{s_{NN}} = 54.4$  and 27 GeV. The bottom panel shows the thermal dielectron mass spectra from 54.4 GeV (red squares) and 27 GeV (black dots) compared to the NA60 thermal dimuon data (magenta inverted triangles).  $M_{ll}$  denotes the invariant mass of dielectron ( $e^+e^-$ ) or dimuon ( $\mu^+\mu^-$ ) pairs. Dashed lines show the fitting curves for the corresponding temperature extractions. Dot-dashed lines display the expected vacuum  $\rho$  spectra ( $f^{BW}(M)$ ) based on the  $p+p$ <sup>46</sup> and  $e^+e^-$ <sup>47</sup> collision data. Vertical bars and boxes around data points represent the statistical and systematic uncertainties, respectively.

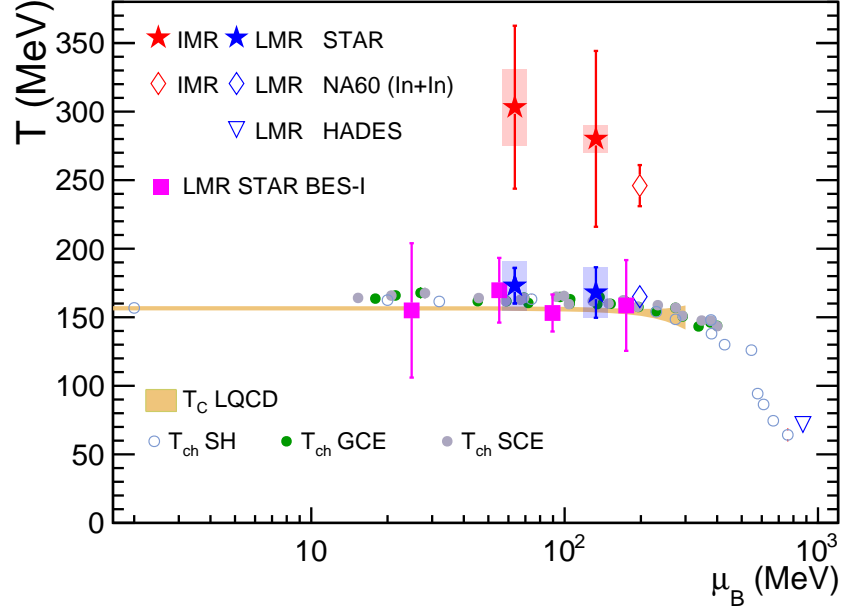


Figure 4: **Temperatures vs. baryon chemical potential.** Temperatures extracted from in-medium  $\rho^0$ ; the region of the later QGP stage (blue stars), and the region of the earlier QGP stage (red stars) from STAR data are compared to the temperatures extracted from NA60 data <sup>35</sup> (diamonds) and HADES data <sup>32</sup> (inverted triangle). Chemical freeze-out temperatures extracted from the statistical thermal models (SH, GCE, SCE) <sup>16,52</sup> are shown as open and filled circles. The QCD critical temperature  $T_C$  at finite  $\mu_B$  predicted by LQCD calculations <sup>17</sup> is shown as a yellow band. All temperatures are plotted at the  $\mu_B$  determined at chemical freeze-out. Vertical bars and boxes around the data points represent the statistical and systematic uncertainties, respectively.

## Methods

**Data description** The thermal dielectron measurements are based on the datasets collected with the STAR detector in Au+Au collisions at  $\sqrt{s_{\text{NN}}} = 27$  GeV (year 2018) and 54.4 GeV (year 2017), using the minimum-bias (MB) trigger which requires a coincidence of signals in the opposite beam-going direction ( $-z$  and  $+z$ ) components of either the Vertex Position Detector <sup>56</sup>(VPD,  $4.25 < |\eta| < 5.1$ ), Beam-Beam Counters <sup>57</sup> (BBC,  $2.2 < |\eta| < 5.0$ ) or the Zero Degree Calorimeters <sup>58</sup> (ZDC,  $|\eta| > 6.0$ ). To ensure the quality of event reconstruction, requirements on the primary vertex reconstructed via the Time Projection Chamber <sup>42</sup> (TPC) detector along the beam axis ( $|V_z^{\text{TPC}}| < 35$  cm) and the transverse radial axis ( $V_r^{\text{TPC}} < 2$  cm) are applied. For the pile-up event rejection, correlations between the number of hits in the Time Of Flight <sup>59</sup> (TOF) and the reference multiplicity of TPC tracks are considered for  $\sqrt{s_{\text{NN}}} = 27$  GeV data, while the difference between  $V_z^{\text{TPC}}$  and  $V_z^{\text{VPD}}$  measured by the VPD is required to be within 3 cm for  $\sqrt{s_{\text{NN}}} = 54.4$  GeV data. There are 256M and 500M events for  $\sqrt{s_{\text{NN}}} = 27$  GeV and 54.4 GeV Au+Au collisions, respectively, that satisfy the event selections.

**Reconstruction of  $e^+e^-$  pairs** The electrons and positrons are identified via the TPC detector (tracking, momentum and  $dE/dx$ ) and TOF detector (time), as described in Refs. <sup>37,38</sup>. These electrons and positrons are required to be within the STAR detector acceptance of pseudo-rapidity ( $|\eta^e| < 1$ ) and transverse momentum ( $p_{\text{T}}^e > 0.2$  GeV/ $c$ ). The selected electrons and positrons from the same events are combined to reconstruct the unlike-sign dielectron ( $e^+e^-$ ) pairs. The raw yields of these inclusive  $e^+e^-$  pairs are denoted as  $N_{+-}$ . The background in the inclusive unlike-sign pairs arises from uncorrelated (random combinatorial) and correlated background (e.g. jet

fragmentation) pairs<sup>60</sup>. These background contributions can be well reproduced by the geometric mean of the like-sign pairs  $N_{\text{geomLS}} = 2\sqrt{N_{++} \times N_{--}}$  as demonstrated in Ref.<sup>60</sup>, where the  $N_{++}$  and  $N_{--}$  represent the raw yields of the like-sign pairs  $e^+e^+$  and  $e^-e^-$  reconstructed by electrons or positrons in the same event. The background pairs from photon conversion in the detector materials are removed by the  $\phi_V$  angle selection method developed by the PHENIX Collaboration<sup>60</sup>. The raw yield of inclusive dielectron signals can be calculated as:

$$N_{\text{raw}} = N_{+-} - N_{\text{geomLS}} \times f_{\text{sign}}, \quad (1)$$

where  $f_{\text{sign}}$  is a correction factor accounting for the differences of detector acceptance between unlike-sign and like-sign particle pairs due to the magnetic field. This factor is evaluated by the ratio of the unlike-sign to the like-sign pairs using event mixing techniques<sup>38,60</sup>,

$$f_{\text{sign}} = \frac{B_{+-}}{2\sqrt{B_{++}B_{--}}}, \quad (2)$$

where  $B_{+-}$ ,  $B_{++}$  and  $B_{--}$  represent the number of unlike-sign pairs and like-sign pairs in the mixed events, respectively.  $B$  and  $N$  are measured as 2-dimensional functions of  $M_{ee}$  and  $p_T$ .

**Efficiency and acceptance corrections** In this study, the single electron reconstruction efficiency includes the tracking reconstruction efficiency (TPC) and the electron identification efficiency (TPC and TOF). The tracking efficiency is evaluated using Monte Carlo simulation embedding techniques, while the electron identification efficiency is determined using data-driven techniques as described in Ref.<sup>38</sup>. The dielectron pair reconstruction efficiency correction ( $\epsilon^{\text{pair}}$ ) and ac-



ceptance correction ( $\text{Acc}^{\text{pair}}$ ) are calculated through the virtual photon decay simulation. This simulation incorporates all the single-electron efficiencies for each daughter particle in a full 3D momentum space of  $(p_T, \eta, \phi)$ . The pair reconstruction efficiency and acceptance corrections are calculated and then applied to correct the raw signal yields in 2D ( $M_{ee}$  vs.  $p_T$ ). The corrected data are normalized by the number of events used for the raw data reconstruction to obtain the invariant yields, which represent the production rate of the reconstructed signal per Au+Au collision in a given centrality class. The correction factors for the dielectron pair efficiency and acceptance are displayed in Extended Data Fig. 1.

**Physics background from non-thermal sources** The background of dielectron pairs from non-thermal physics sources (conventionally named cocktails “CKT”) is determined through cocktail simulation techniques <sup>38,60</sup>. This process is accomplished through two major steps: (1) simulating the invariant mass lineshapes through the dielectron decay channel, and (2) scaling their contributions by their invariant yields. In the simulations, the detector acceptance and momentum resolution are incorporated into the simulations of hadron decays to accurately reproduce the background in real data. Long-lived light hadrons such as  $\pi^0$ ,  $\eta$ ,  $\eta'$ ,  $\omega$ , and  $\phi$  preserve their vacuum decay structures as they decay after the kinetic freeze-out of the collision system. The  $p_T$  spectra of light hadrons are determined through the Tsallis Blast-Wave (TBW) model <sup>61</sup>, which is fit to STAR’s measured light hadron production <sup>52</sup>. The rapidity distribution of light hadrons is determined through the GENESIS event generator <sup>62</sup>, parameterized to match CERN SPS data <sup>63–66</sup>. The  $J/\psi$  vector meson has a much longer lifetime ( $\sim 2 \times 10^3$  fm/c) compared to the typical medium lifetime ( $\sim 10$  fm/c), ensuring that almost all the  $J/\psi$  decay in vacuum, regardless of their produc-

tion timing. The  $p_T$  spectra of the  $J/\psi$  are obtained from STAR published data <sup>67</sup>. After the mass lineshapes of the physics background sources are determined, the next step is to scale them with the invariant yields. The  $\pi^0$  yields are determined by averaging  $\pi^\pm$  from high-precision STAR data <sup>52</sup>. The invariant yield ratios  $\sigma_\eta/\sigma_{\pi^0}$  and  $\sigma_{\eta'}/\sigma_{\pi^0}$  are taken from experimental data <sup>60,68–70</sup>. The invariant yields of  $\omega$ ,  $\phi$ , and  $J/\psi$  mesons are determined in this study by taking into account the distinct differences in their mass lineshapes compared to the smooth thermal dielectron mass spectra. In particular, considering that  $\omega$  and  $\phi$  are very close to the in-medium  $\rho$  signals, theoretical lineshapes from the Rapp Model and the simulated  $\omega$  and  $\phi$  lineshapes are fit to data to determine their yields.

The semi-leptonic decays of charmed hadrons are a special type of physics background. In heavy-ion collisions, charm and anti-charm quarks are created in pairs through initial hard interactions and then form charmed and anti-charmed hadrons with long lifetimes of  $O(100) \mu\text{m}/c$ . When these hadrons decay, they produce electrons and positrons through semi-leptonic decay in vacuum. The invariant mass spectra from these electron-positron pairs are distributed smoothly and are expected to contribute significantly in the mass range of 1-3  $\text{GeV}/c^2$ . The contribution from open charm decays is simulated in  $p+p$  collisions using PYTHIA v6.416 <sup>71</sup>, with the settings described in Ref. <sup>72</sup>. The total cross section for charm production per nucleon-nucleon collision has been measured worldwide as a function of the center-of-mass energy  $\sqrt{s}$ , and the results are presented in Extended Data Figure 2. To estimate the cross section values at  $\sqrt{s} = 27$  and 54.4 GeV, the experimental data are fit with a theoretical curve from NLO pQCD calculations (MNR <sup>73</sup>). To estimate the uncertainties associated with the cross section values, two alternative approaches were

employed to gauge the impact on the default values. Firstly, the NLO pQCD curve fit was applied exclusively to data up to RHIC energies, allowing for an assessment of the exclusion of higher energy data. Secondly, the FONLL curve, as reported in Ref. <sup>74</sup>, was directly utilized to give the extrapolations. The differences arising from these two approaches in comparison to the default values were incorporated into the total uncertainties of the cross section values. The resulting values and the associated uncertainties of  $\sigma_{c\bar{c}}^{\text{NN}}$  are  $16.7 \pm 3.3 \mu\text{b}$  and  $72.0 \pm 14.4 \mu\text{b}$  for  $\sqrt{s} = 27 \text{ GeV}$  and  $54.4 \text{ GeV}$ , respectively. The contribution from the Drell-Yan process is simulated for the  $p+p$  collisions using mainly the same PYTHIA v6.416 settings as in a previous study <sup>72</sup>, while the  $k_T$  is tuned to be  $0.95 \text{ GeV}/c$  to match the measured Drell-Yan  $p_T$  spectrum from the FNAL-288 experiment <sup>75</sup> in the mass region of  $5\text{-}9 \text{ GeV}/c^2$ . The total production cross section of  $c\bar{c}$  and Drell-Yan process for Au+Au collisions is calculated by multiplying the number of nucleon-nucleon binary collisions ( $N_{\text{coll}}$ ), as obtained from a Glauber Model <sup>76</sup>.

**Thermal  $e^+e^-$  spectrum** The thermal dielectron spectra are determined by subtracting all the physics background from the inclusive dielectron spectra with

$$\begin{aligned}
 N_{\text{thermal}} &= \left( \frac{1}{N_{\text{event}}} \times \frac{N_{\text{raw}}}{\epsilon^{\text{pair}}} - N_{\text{CKTSum}}^{\text{inAcc}} \right) \times \frac{1}{\text{Acc}^{\text{pair}}} \\
 &= N_{\text{FullCorr}} - N_{\text{CKTSum}},
 \end{aligned}
 \tag{3}$$

where  $N_{\text{thermal}}$ ,  $N_{\text{FullCorr}}$  and  $N_{\text{CKTSum}}$  represent the number of pairs from the thermal dielectron, the fully corrected inclusive dielectron and the total physics backgrounds. The  $N_{\text{CKTSum}}^{\text{inAcc}}$  represents the amount of physics background within the STAR acceptance. The thermal dielectron production spectra are studied in various Au+Au collision centralities including the 0-80% centrality and the sub-centralities (0-10%, 10-40%, 40-80%). For each given centrality bin, the dielectron signals,

the efficiency corrections, and its cocktail simulations are carried out individually for the final thermal dielectron spectrum determination.

**Systematic uncertainties** In thermal dielectron spectrum measurements and temperature measurements, the sources of systematic uncertainties arise from both measurements of data and estimation of physics background, respectively. The systematic uncertainties from experimental data include the efficiency corrections of single electron reconstruction and the dielectron pair reconstruction, which are estimated by methods similar to those described in Refs. <sup>37,38</sup>. The systematic uncertainties from the physics background contributions have three primary sources: the invariant yields, the branching ratios of hadrons that decay into  $e^+e^-$ , and the de-correlation effects on the mass distribution of the  $c$  and  $\bar{c}$  decayed dielectron pairs due to potential medium modifications. The uncertainties associated with the invariant yields of  $\pi^0$ ,  $\eta$ ,  $\eta'$  are established based on previous experimental data <sup>38,52,77</sup> while the uncertainties for vector mesons ( $\omega$ ,  $\phi$  and  $J/\psi$ ) are determined in this study.

The uncertainties in the  $c\bar{c}$  yields are determined from two sources: the extrapolation of worldwide data and the values of  $N_{\text{coll}}$ . For the Drell-Yan production, the uncertainty is estimated by considering the uncertainties in PYTHIA simulations and in the values of  $N_{\text{coll}}$ . The  $c\bar{c}$  pairs are largely produced as back-to-back pairs via the initial hard scatterings. However, interactions with the hot QCD medium at later stages can modify their kinematics, resulting in de-correlation effects on their decayed  $e^+e^-$  pairs, which affects their reconstructed invariant mass distribution. To address these de-correlation effects, given the poorly known medium modifications, two extreme conditions are considered for systematic uncertainty estimation: (1) the angles of the single

electron and positron are randomly assigned for their pair mass calculation, which effectively eliminates their correlations; (2) re-weight the  $p_T$  of these  $e^+$  and  $e^-$  with the theoretical predictions from the Duke model <sup>78</sup> and the PHSD model <sup>79,80</sup> taking into account the strong interactions between charm quarks and the medium during the system evolution for the 200 GeV Au+Au collisions, where the medium modification effects are expected to be stronger than at 27 GeV and 54.4 GeV.

The systematic uncertainties on the thermal dielectron mass spectrum and the extracted temperatures are evaluated separately for individual sources by considering the variations with respect to their default values. The total systematic uncertainties are then determined by combining the individual uncertainties in quadrature. The primary source of systematic uncertainty on the fully corrected dielectron mass spectrum is due to uncertainties in the single electron reconstruction efficiencies. These uncertainties are  $\sim 7-10\%$  for both the 27 and 54.4 GeV data sets, resulting in systematic uncertainties of roughly 10-20% and 40-45% for the thermal dielectron mass spectrum at 27 and 54.4 GeV, respectively. However, these uncertainties have minimal impact (1-2%) on the temperature extraction as they are largely correlated across mass bins and hence do not significantly distort the shape of the mass distribution. The dominant source of mass-dependent systematic uncertainty for the thermal dielectron mass spectrum is due to the simulation of cocktail tails. This leads to uncertainties of about 10-50% in the LMR and 10-20% in the IMR for the 27 GeV data, and 10-60% in the LMR and 10-30% in the IMR for the 54.4 GeV data. This source of uncertainty also dominates the systematic uncertainty of temperature measurements in the LMR at  $\sim 10\%$ . The systematic uncertainty of temperatures from the IMR is found to be less than 10%,

due to the relatively higher ratio of Data/CKTSum and smoother systematic uncertainties of the thermal dielectron mass spectrum.

**Centrality definition** In heavy-ion collisions, centrality is a physics quantity that quantifies the extent of overlap between the colliding nuclei. In this study, centrality is determined by aligning Monte Carlo Glauber simulations with the distributions of charged tracks in Au+Au collisions reconstructed in the STAR TPC, employing the methodologies described in Ref. <sup>76</sup>. The Au+Au collisions are classified into centrality intervals, presented as percentages of the total nucleus-nucleus inelastic interaction cross section. A smaller (larger) percentage corresponds to more central (peripheral) collisions.

**Data compared to theoretical models** Theoretical calculations from the Rapp model <sup>13,14,29,81</sup> and the PHSD model <sup>26,27</sup> have successfully reproduced previous thermal dilepton measurements in both SPS and RHIC heavy-ion collisions. As shown in the Extended Data Fig. 3 and Fig. 4, both models are compared to the spectra measured at STAR from 27 GeV and 54.4 GeV data in the different centralities. In general, both models can well describe the experimental data while the PHSD model seems to underestimate the data from the most peripheral Au+Au collisions (40-80% centrality) at 54.4 GeV.

**Temperatures at different centrality** To study the centrality dependence of the created thermal QCD medium, the associated thermal emission temperatures are extracted from the thermal dielectron spectrum in different centralities. The extracted temperatures from both LMR and IMR are presented as a function of  $N_{\text{part}}$ , as shown in the Extended Data Fig. 5. In general, the temperatures

at different centralities are consistent within uncertainties for both  $T_{\text{LMR}}$  and  $T_{\text{IMR}}$ . Moreover, the temperatures from 27 GeV and 54.4 GeV Au+Au collisions are consistent for all centralities. Temperatures extracted from the LMR tend to cluster around the critical temperature from lattice QCD calculations. On the other hand, temperatures extracted in the IMR are generally higher than  $T_{\text{LMR}}$  and  $T_C$ .

**Thermal lepton yield** The Extended Data Fig. 6 shows the thermal dilepton yields integrated over  $0.4 < M_{ll} < 0.75 \text{ GeV}/c^2$  as a function of the collision energy. These yields are divided by the average charged particle density to cancel out collision system volume effects. As the data show, the normalized thermal dilepton yields from the 0-80% centrality show no clear dependence on the collision energy. To directly prove that these thermal dileptons are emitted at an early stage of a collision when the system can be described as a hot QCD medium, the measured thermal dilepton yields are compared to the predictions from a statistical thermal model, as well as the  $\rho^0 \rightarrow e^+e^-$  converted from the measured  $\rho^0 \rightarrow \pi^+\pi^-$ . The later is carried out with the data from  $p+p$  collisions<sup>46,82-84</sup>,  $e^+e^-$  collisions<sup>47,85,86</sup> and peripheral Au+Au collisions<sup>50</sup> by considering the decay branching ratios of  $\rho^0$  to  $e^+e^-$  ( $4.72 \times 10^{-5}$ ) and to  $\pi^+\pi^-$  ( $\sim 100\%$ ). In principle, these converted data can also represent the expected dielectron yields decayed from  $\rho^0$  at chemical freeze-out. As one can see, the thermal dielectron yields are generally a factor of 5 higher than those expected from the chemical freeze-out. In order to investigate the impact of mass on the  $\rho^0$  yield at chemical freeze-out, the statistical thermal model calculation with the  $\rho^0$  pole mass altered to  $0.4 \text{ GeV}/c^2$  is performed for this particular study and shown as a dashed line. As one can see, all the above comparisons provide solid evidence that the measured thermal dielectrons

are predominantly from the stage when the collision system stays as a thermal hadronic/partonic source.

**Temperature extraction with thermal dilepton mass spectra from NA60 data** In 2009, the NA60 collaboration published the most precise thermal dilepton data for In+In collisions at  $\sqrt{s_{\text{NN}}} = 17.3$  GeV. Here, we perform a temperature extraction based on the same method as described in the main text using the NA60 collaboration data published in Refs. <sup>34,35,87</sup>. The fitting results are shown in the Extended Data Fig. 7. Note that the IMR data from Fig. 4.5 is used here, instead of that from Fig. 5.1 in Ref <sup>35</sup>, because the former includes the systematic uncertainties. Temperature values from NA60 LMR and IMR data are extracted as  $T_{\text{LMR}} = 165 \pm 4$  MeV and  $T_{\text{IMR}} = 245 \pm 17$  MeV, respectively. We also note that the temperature is found to be  $T_{\text{LMR}} = 151 \pm 2$  MeV when fitting to the LMR data from the NA60 Hard Probes conference proceedings <sup>88</sup>.

1. Shuryak, E. V. Quark-Gluon Plasma and Hadronic Production of Leptons, Photons and Psions. *Phys. Lett. B* **78**, 150 (1978).
2. Gross, D. J., Pisarski, R. D. & Yaffe, L. G. QCD and Instantons at Finite Temperature. *Rev. Mod. Phys.* **53**, 43 (1981).
3. Linde, A. D. Phase Transitions in Gauge Theories and Cosmology. *Rept. Prog. Phys.* **42**, 389 (1979).
4. Roberts, C. D. & Schmidt, S. M. Dyson-Schwinger equations: Density, temperature and continuum strong QCD. *Prog. Part. Nucl. Phys.* **45**, S1–S103 (2000). nucl-th/0005064.



5. Olive, K. A. The Quark - hadron transition in cosmology and astrophysics. *Science* **251**, 1194–1199 (1991).
6. Schwarz, D. J. The first second of the universe. *Annalen Phys.* **12**, 220–270 (2003). astro-ph/0303574.
7. Boyanovsky, D., de Vega, H. J. & Schwarz, D. J. Phase transitions in the early and the present universe. *Ann. Rev. Nucl. Part. Sci.* **56**, 441–500 (2006). hep-ph/0602002.
8. Fischer, T. *et al.* Quark deconfinement as a supernova explosion engine for massive blue supergiant stars. *Nature Astron.* **2**, 980–986 (2018). 1712.08788.
9. Baym, G. *et al.* From hadrons to quarks in neutron stars: a review. *Rept. Prog. Phys.* **81**, 056902 (2018). 1707.04966.
10. Annala, E., Gorda, T., Kurkela, A., Nättilä, J. & Vuorinen, A. Evidence for quark-matter cores in massive neutron stars. *Nature Phys.* **16**, 907–910 (2020). 1903.09121.
11. Braun-Munzinger, P., Koch, V., Schäfer, T. & Stachel, J. Properties of hot and dense matter from relativistic heavy ion collisions. *Phys. Rept.* **621**, 76–126 (2016). 1510.00442.
12. Busza, W., Rajagopal, K. & van der Schee, W. Heavy Ion Collisions: The Big Picture, and the Big Questions. *Ann. Rev. Nucl. Part. Sci.* **68**, 339–376 (2018). 1802.04801.
13. van Hees, H. & Rapp, R. Comprehensive interpretation of thermal dileptons at the SPS. *Phys. Rev. Lett.* **97**, 102301 (2006). hep-ph/0603084.

14. Rapp, R. & van Hees, H. Thermal Dileptons as Fireball Thermometer and Chronometer. *Phys. Lett. B* **753**, 586–590 (2016). 1411.4612.
15. Shen, C., Heinz, U. W., Paquet, J.-F. & Gale, C. Thermal photons as a quark-gluon plasma thermometer reexamined. *Phys. Rev. C* **89**, 044910 (2014). 1308.2440.
16. Andronic, A., Braun-Munzinger, P., Redlich, K. & Stachel, J. Decoding the phase structure of QCD via particle production at high energy. *Nature* **561**, 321–330 (2018). 1710.09425.
17. Bazavov, A. *et al.* Chiral crossover in QCD at zero and non-zero chemical potentials. *Phys. Lett. B* **795**, 15–21 (2019). 1812.08235.
18. Borsanyi, S. *et al.* QCD Crossover at Finite Chemical Potential from Lattice Simulations. *Phys. Rev. Lett.* **125**, 052001 (2020). 2002.02821.
19. McLerran, L. D. & Toimela, T. Photon and Dilepton Emission from the Quark - Gluon Plasma: Some General Considerations. *Phys. Rev. D* **31**, 545 (1985).
20. Shuryak, E. V. & Xiong, L. Dilepton and photon production in the ‘hot glue’ scenario. *Phys. Rev. Lett.* **70**, 2241–2244 (1993). hep-ph/9301218.
21. Stoecker, H. & Greiner, W. High-Energy Heavy Ion Collisions: Probing the Equation of State of Highly Excited Hadronic Matter. *Phys. Rept.* **137**, 277–392 (1986).
22. Adare, A. *et al.* Centrality dependence of low-momentum direct-photon production in Au+Au collisions at  $\sqrt{s_{NN}} = 200$  GeV. *Phys. Rev. C* **91**, 064904 (2015). 1405.3940.

23. Adam, J. *et al.* Direct photon production in Pb-Pb collisions at  $\sqrt{s_{\text{NN}}} = 2.76$  TeV. *Phys. Lett. B* **754**, 235–248 (2016). 1509.07324.
24. Acharya, U. A. *et al.* Nonprompt direct-photon production in Au+Au collisions at  $\sqrt{s_{\text{NN}}} = 200$  GeV (2022). 2203.17187.
25. Abdulameer, N. J. *et al.* Low-pT direct-photon production in Au+Au collisions at  $\sqrt{s_{\text{NN}}} = 39$  and 62.4 GeV. *Phys. Rev. C* **107**, 024914 (2023). 2203.12354.
26. Cassing, W., Bratkovskaya, E. L., Rapp, R. & Wambach, J. Probing the rho spectral function in hot and dense nuclear matter by dileptons. *Phys. Rev. C* **57**, 916–921 (1998). nucl-th/9708020.
27. Cassing, W. & Bratkovskaya, E. L. Hadronic and electromagnetic probes of hot and dense nuclear matter. *Phys. Rept.* **308**, 65–233 (1999).
28. Rapp, R. & Wambach, J. Chiral symmetry restoration and dileptons in relativistic heavy ion collisions. *Adv. Nucl. Phys.* **25**, 1 (2000). hep-ph/9909229.
29. Rapp, R. Signatures of thermal dilepton radiation at RHIC. *Phys. Rev. C* **63**, 054907 (2001). hep-ph/0010101.
30. Schnedermann, E., Sollfrank, J. & Heinz, U. W. Thermal phenomenology of hadrons from 200 A GeV S+S collisions. *Phys. Rev. C* **48**, 2462–2475 (1993). nucl-th/9307020.
31. Roche, G. *et al.* Dielectron Production in Ca+Ca Collisions at 1 A GeV and 2 A GeV. *Phys. Lett. B* **226**, 228–232 (1989).

32. Adamczewski-Musch, J. *et al.* Probing dense baryon-rich matter with virtual photons. *Nature Phys.* **15**, 1040–1045 (2019).
33. Adamova, D. *et al.* Enhanced production of low mass electron pairs in 40 A GeV Pb-Au collisions at the CERN SPS. *Phys. Rev. Lett.* **91**, 042301 (2003). nucl-ex/0209024.
34. Arnaldi, R. *et al.* Evidence for radial flow of thermal dileptons in high-energy nuclear collisions. *Phys. Rev. Lett.* **100**, 022302 (2008). 0711.1816.
35. Arnaldi, R. *et al.* Evidence for the production of thermal-like muon pairs with masses above 1 GeV/c<sup>2</sup> in 158 A GeV Indium-Indium Collisions. *Eur. Phys. J. C* **59**, 607–623 (2009). 0810.3204.
36. Adamczyk, L. *et al.* Dielectron Mass Spectra from Au+Au Collisions at  $\sqrt{s_{\text{NN}}} = 200$  GeV. *Phys. Rev. Lett.* **113**, 022301 (2014). [Addendum: *Phys.Rev.Lett.* 113, 049903 (2014)], 1312.7397.
37. Adamczyk, L. *et al.* Energy dependence of acceptance-corrected dielectron excess mass spectrum at mid-rapidity in Au+Au collisions at  $\sqrt{s_{\text{NN}}} = 19.6$  and 200 GeV. *Phys. Lett. B* **750**, 64–71 (2015). 1501.05341.
38. Adamczyk, L. *et al.* Measurements of Dielectron Production in Au+Au Collisions at  $\sqrt{s_{\text{NN}}} = 200$  GeV from the STAR Experiment. *Phys. Rev. C* **92**, 024912 (2015). 1504.01317.
39. Abdulhamid, M. I. *et al.* Measurements of dielectron production in Au+Au collisions at  $\sqrt{s_{\text{NN}}} = 27, 39,$  and 62.4 GeV from the STAR experiment. *Phys. Rev. C* **107**, L061901 (2023).

40. Adare, A. *et al.* Dielectron production in Au+Au collisions at  $\sqrt{s_{\text{NN}}} = 200$  GeV. *Phys. Rev. C* **93**, 014904 (2016). 1509.04667.
41. Acharya, S. *et al.* Measurement of dielectron production in central Pb-Pb collisions at  $\sqrt{s_{\text{NN}}} = 2.76$  TeV. *Phys. Rev. C* **99**, 024002 (2019). 1807.00923.
42. Anderson, M. *et al.* The Star time projection chamber: A Unique tool for studying high multiplicity events at RHIC. *Nucl. Instrum. Meth. A* **499**, 659–678 (2003). nucl-ex/0301015.
43. Shao, M. *et al.* Extensive particle identification with TPC and TOF at the STAR experiment. *Nucl. Instrum. Meth. A* **558**, 419–429 (2006). nucl-ex/0505026.
44. Kenyon, I. R. The Drell-Yan Process. *Rept. Prog. Phys.* **45**, 1261 (1982).
45. Dalitz, R. H. On an alternative decay process for the neutral  $\pi$  meson, Letters to the Editor. *Proc. Phys. Soc. A* **64**, 667–669 (1951).
46. Aguilar-Benitez, M. *et al.* Inclusive particle production in 400 GeV p+p interactions. *Z. Phys. C* **50**, 405–426 (1991).
47. Derrick, M. *et al.* Neutral  $K^*$  (890) and  $\rho^0$  Meson Production in  $e^+e^-$  Annihilation at the  $\sqrt{s} = 29$  GeV. *Phys. Lett. B* **158**, 519–524 (1985).
48. Adler, C. *et al.* Coherent  $\rho^0$  production in ultraperipheral heavy ion collisions. *Phys. Rev. Lett.* **89**, 272302 (2002). nucl-ex/0206004.
49. Shuryak, E. V. & Brown, G. E. Matter induced modification of resonances at RHIC freezeout. *Nucl. Phys. A* **717**, 322–335 (2003). hep-ph/0211119.

50. Adams, J. *et al.*  $\rho^0$  production and possible modification in Au+Au and p+p collisions at  $\sqrt{s_{\text{NN}}} = 200$  GeV. *Phys. Rev. Lett.* **92**, 092301 (2004). nucl-ex/0307023.
51. Kasmaei, B. S. & Strickland, M. Dilepton production and elliptic flow from an anisotropic quark-gluon plasma. *Phys. Rev. D* **99**, 034015 (2019). 1811.07486.
52. Adamczyk, L. *et al.* Bulk Properties of the Medium Produced in Relativistic Heavy-Ion Collisions from the Beam Energy Scan Program. *Phys. Rev. C* **96**, 044904 (2017). 1701.07065.
53. Savchuk, O. *et al.* Enhanced dilepton emission from a phase transition in dense matter. *J. Phys. G* **50**, 125104 (2023). 2209.05267.
54. Rischke, D. H. & Gyulassy, M. The time delay signature of quark-gluon plasma formation in relativistic nuclear collisions. *Nucl. Phys. A* **608**, 479–512 (1996). nucl-th/9606039.
55. Nara, Y. & Ohnishi, A. Mean-field update in the JAM microscopic transport model: Mean-field effects on collective flow in high-energy heavy-ion collisions at  $s_{\text{NN}}=2\text{--}20$  GeV energies. *Phys. Rev. C* **105**, 014911 (2022). 2109.07594.
56. Llope, W. J. *et al.* The STAR Vertex Position Detector. *Nucl. Instrum. Meth. A* **759**, 23–28 (2014). 1403.6855.
57. Whitten, C. A. The beam-beam counter: A local polarimeter at STAR. *AIP Conf. Proc.* **980**, 390–396 (2008).
58. Adler, C. *et al.* The RHIC zero degree calorimeter. *Nucl. Instrum. Meth. A* **470**, 488–499 (2001). nucl-ex/0008005.

59. Llope, W. J. Multigap RPCs in the STAR experiment at RHIC. *Nucl. Instrum. Meth. A* **661**, S110–S113 (2012).
60. Adare, A. *et al.* Detailed measurement of the  $e^+e^-$  pair continuum in  $p + p$  and Au+Au collisions at  $\sqrt{s_{\text{NN}}} = 200$  GeV and implications for direct photon production. *Phys. Rev. C* **81**, 034911 (2010). 0912.0244.
61. Chen, J., Deng, J., Tang, Z., Xu, Z. & Yi, L. Nonequilibrium kinetic freeze-out properties in relativistic heavy ion collisions from energies employed at the RHIC beam energy scan to those available at the LHC. *Phys. Rev. C* **104**, 034901 (2021). 2012.02986.
62. T. Ullrich, D. I. *et al.* Development of new genesis. *GSI Technical Report* **03-24** (2000).
63. Aggarwal, M. M. *et al.* Transverse mass distributions of neutral pions from Pb-208 induced reactions at 158-A GeV. *Eur. Phys. J. C* **23**, 225–236 (2002). nucl-ex/0108006.
64. Aggarwal, M. M. *et al.* Centrality dependence of neutral pion production in 158-A GeV Pb-208 + Pb-208 collisions. *Phys. Rev. Lett.* **81**, 4087–4091 (1998). [Erratum: *Phys.Rev.Lett.* 84, 578–579 (2000)], nucl-ex/9806004.
65. Humanic, T. J. Recent results from the CERN NA44 experiment. *Int. J. Mod. Phys. A* **16S1C**, 1257–1259 (2001).
66. Roland, G. *et al.* Recent results on central Pb + Pb collisions from experiment NA49. *Nucl. Phys. A* **638**, 91–102 (1998).

67. Adamczyk, L. *et al.* Energy dependence of  $J/\psi$  production in Au+Au collisions at  $\sqrt{s_{\text{NN}}} = 39, 62.4$  and  $200$  GeV. *Phys. Lett. B* **771**, 13–20 (2017). 1607.07517.
68. Adler, S. S. *et al.* High transverse momentum  $\eta$  meson production in  $p+p$ ,  $d+\text{Au}$  and Au+Au collisions at  $\sqrt{s_{\text{NN}}} = 200$  GeV. *Phys. Rev. C* **75**, 024909 (2007). nucl-ex/0611006.
69. Aggarwal, M. M. *et al.* Direct photon production in 158-A GeV Pb-208 + Pb-208 collisions (2000). nucl-ex/0006007.
70. Adamczyk, L. *et al.* Di-electron spectrum at mid-rapidity in  $p + p$  collisions at  $\sqrt{s} = 200$  GeV. *Phys. Rev. C* **86**, 024906 (2012). 1204.1890.
71. Sjostrand, T. *et al.* High-energy physics event generation with PYTHIA 6.1. *Comput. Phys. Commun.* **135**, 238–259 (2001). hep-ph/0010017.
72. Agakishiev, H. *et al.* High  $p_T$  non-photon electron production in  $p+p$  collisions at  $\sqrt{s} = 200$  GeV. *Phys. Rev. D* **83**, 052006 (2011). 1102.2611.
73. Mangano, M. L., Nason, P. & Ridolfi, G. Heavy quark correlations in hadron collisions at next-to-leading order. *Nucl. Phys. B* **373**, 295–345 (1992).
74. Nelson, R. E., Vogt, R. & Frawley, A. D. Narrowing the uncertainty on the total charm cross section and its effect on the  $J/\psi$  cross section. *Phys. Rev. C* **87**, 014908 (2013). 1210.4610.
75. Ito, A. S. *et al.* Measurement of the Continuum of Dimuons Produced in High-Energy Proton - Nucleus Collisions. *Phys. Rev. D* **23**, 604–633 (1981).



76. Miller, M. L., Reygers, K., Sanders, S. J. & Steinberg, P. Glauber modeling in high energy nuclear collisions. *Ann. Rev. Nucl. Part. Sci.* **57**, 205–243 (2007). nucl-ex/0701025.
77. Abelev, B. I. *et al.* Systematic Measurements of Identified Particle Spectra in  $pp$ ,  $d^+$  Au and Au+Au Collisions from STAR. *Phys. Rev. C* **79**, 034909 (2009). 0808.2041.
78. Cao, S., Qin, G.-Y. & Bass, S. A. Energy loss, hadronization and hadronic interactions of heavy flavors in relativistic heavy-ion collisions. *Phys. Rev. C* **92**, 024907 (2015). 1505.01413.
79. Cassing, W. & Bratkovskaya, E. L. Parton transport and hadronization from the dynamical quasiparticle point of view. *Phys. Rev. C* **78**, 034919 (2008). 0808.0022.
80. Cassing, W. & Bratkovskaya, E. L. Parton-Hadron-String Dynamics: an off-shell transport approach for relativistic energies. *Nucl. Phys. A* **831**, 215–242 (2009). 0907.5331.
81. Rapp, R. & van Hees, H. Thermal Electromagnetic Radiation in Heavy-Ion Collisions. *Eur. Phys. J. A* **52**, 257 (2016). 1608.05279.
82. Blobel, V. *et al.* Observation of Vector Meson Production in Inclusive  $p p$  Reactions. *Phys. Lett. B* **48**, 73–76 (1974).
83. Singer, R. *et al.*  $\rho^0$  Production in 205 GeV/c  $p p$  Interactions. *Phys. Lett. B* **60**, 385–388 (1976).
84. Drijard, D. *et al.* Production of Vector and Tensor Mesons in Proton Proton Collisions at  $\sqrt{s} = 52.5$  GeV. *Z. Phys. C* **9**, 293 (1981).

85. Albrecht, H. *et al.* Inclusive production of  $K^*(892)$ ,  $\rho^0(770)$ , and  $\omega(783)$  mesons in the  $\Upsilon$  energy region. *Z. Phys. C* **61**, 1–18 (1994).
86. Pei, Y.-J. A Simple approach to describe hadron production rates in  $e^+ e^-$  annihilation. *Z. Phys. C* **72**, 39–46 (1996).
87. Arnaldi, R. *et al.* NA60 results on thermal dimuons. *Eur. Phys. J. C* **61**, 711–720 (2009). 0812.3053.
88. Specht, H. J. Thermal Dileptons from Hot and Dense Strongly Interacting Matter. *AIP Conf. Proc.* **1322**, 1–10 (2010). 1011.0615.
89. Abelev, B. *et al.* Measurement of charm production at central rapidity in proton-proton collisions at  $\sqrt{s} = 7$  TeV. *JHEP* **01**, 128 (2012). 1111.1553.
90. Aaij, R. *et al.* Prompt charm production in pp collisions at  $\sqrt{s}=7$  TeV. *Nucl. Phys. B* **871**, 1–20 (2013). 1302.2864.
91. Adamczyk, L. *et al.* Measurements of  $D^0$  and  $D^*$  Production in  $p + p$  Collisions at  $\sqrt{s} = 200$  GeV. *Phys. Rev. D* **86**, 072013 (2012). 1204.4244.
92. Adare, A. *et al.* Heavy Quark Production in  $p + p$  and Energy Loss and Flow of Heavy Quarks in Au+Au Collisions at  $\sqrt{s_{NN}} = 200$  GeV. *Phys. Rev. C* **84**, 044905 (2011). 1005.1627.
93. Aad, G. *et al.* Measurement of  $D^{*\pm}$ ,  $D^\pm$  and  $D_s^\pm$  meson production cross sections in  $pp$  collisions at  $\sqrt{s} = 7$  TeV with the ATLAS detector. *Nucl. Phys. B* **907**, 717–763 (2016). 1512.02913.

94. Alves, G. A. *et al.* Forward cross-sections for production of  $D^+$ ,  $D^0$ ,  $D_s$ ,  $D^{*+}$  and  $\Lambda^c$  in 250 GeV  $\pi^\pm$ ,  $K^\pm$ , and  $p$  nucleon interactions. *Phys. Rev. Lett.* **77**, 2388–2391 (1996). [Erratum: *Phys.Rev.Lett.* 81, 1537 (1998)].
95. Amaryan, M. *et al.* (eds.). *Workshop on Excited Hyperons in QCD Thermodynamics at Freeze-Out (YSTAR2016) Mini-Proceedings (2017)*. 1701.07346.
96. Wheaton, S. & Cleymans, J. THERMUS: A Thermal model package for ROOT. *Comput. Phys. Commun.* **180**, 84–106 (2009). hep-ph/0407174.

**Data availability** All data published in this article are publicly available in the HEPdata repository (<https://hepdata.net/record/xxxxx>).

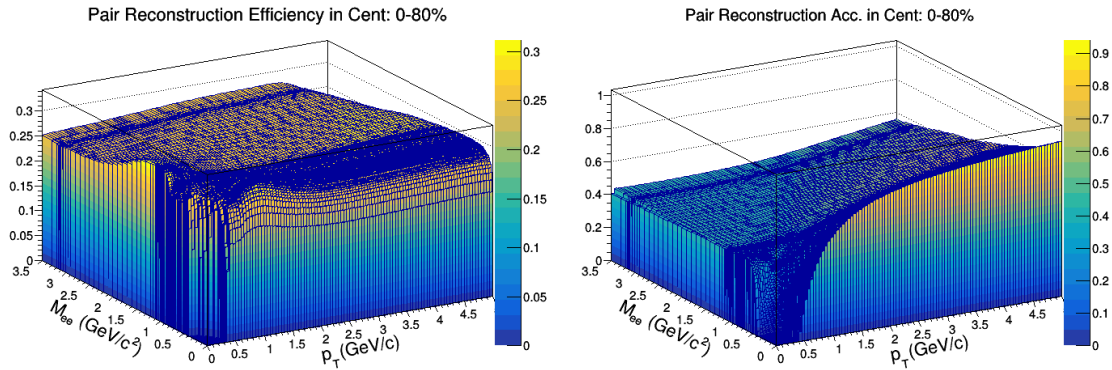
**Codes availability** Codes to process raw data collected by the STAR detector and codes to analyze the produced data are not available to the public.

#### 4 Acknowledgement

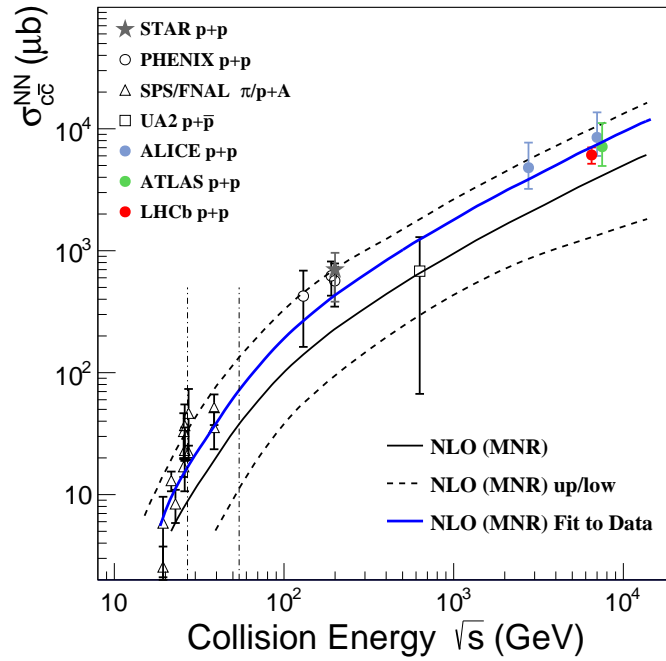
We thank the RHIC Operations Group and RCF at BNL, the NERSC Center at LBNL, and the Open Science Grid consortium for providing resources and support. This work was supported in part by the Office of Nuclear Physics within the U.S. DOE Office of Science, the U.S. National Science Foundation, National Natural Science Foundation of China, Chinese Academy of Science, the Ministry of Science and Technology of China and the Chinese Ministry of Education, the Higher Education Sprout Project by Ministry of Education at NCKU, the National Research Foun-

dation of Korea, Czech Science Foundation and Ministry of Education, Youth and Sports of the Czech Republic, Hungarian National Research, Development and Innovation Office, New National Excellency Programme of the Hungarian Ministry of Human Capacities, Department of Atomic Energy and Department of Science and Technology of the Government of India, the National Science Centre and WUT ID-UB of Poland, the Ministry of Science, Education and Sports of the Republic of Croatia, German Bundesministerium für Bildung, Wissenschaft, Forschung and Technologie (BMBF), Helmholtz Association, Ministry of Education, Culture, Sports, Science, and Technology (MEXT), Japan Society for the Promotion of Science (JSPS) and Agencia Nacional de Investigación y Desarrollo (ANID) of Chile.

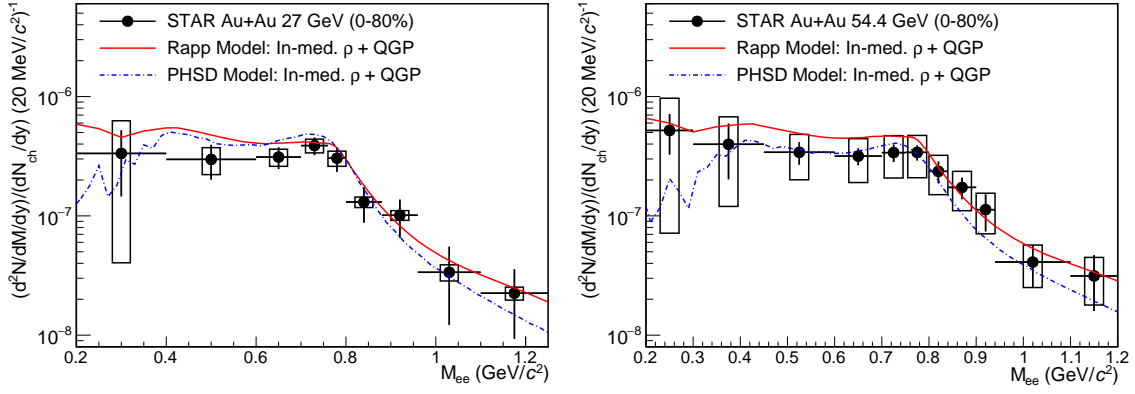
### Extended Data



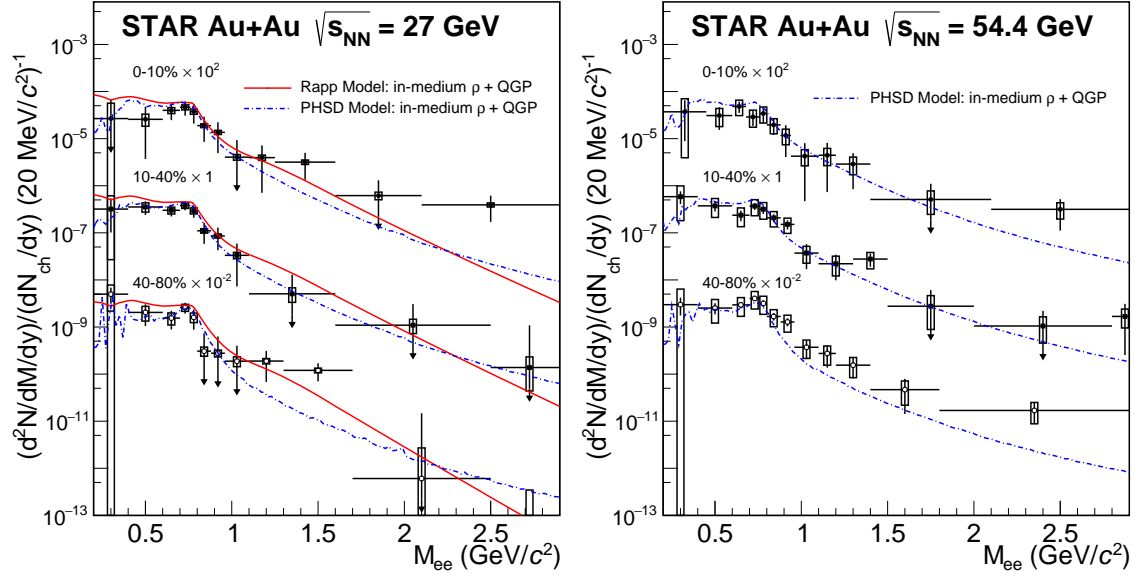
Extended Data Figure 1: Example of dielectron pair reconstruction efficiency (left) and acceptance (right) in 2D ( $M_{ee}, p_T$ ) of  $\sqrt{s_{NN}} = 27$  GeV Au+Au 0-80% centrality collisions



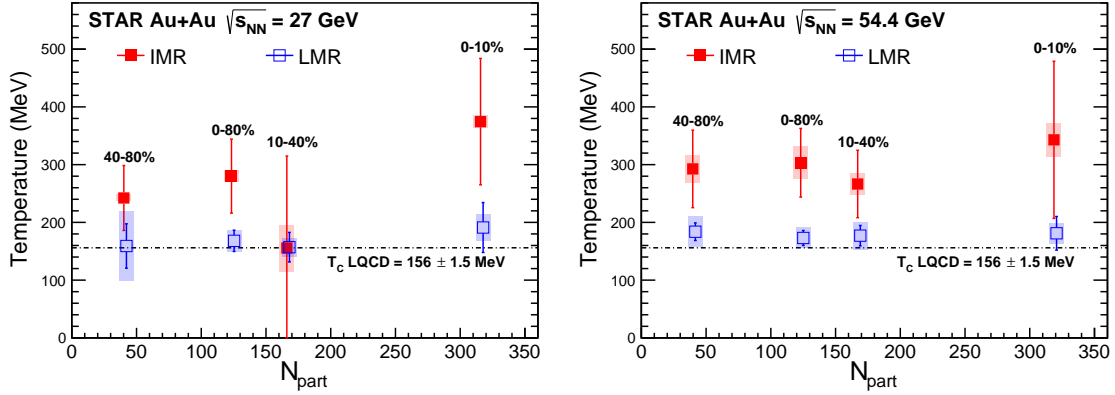
Extended Data Figure 2: Total charm ( $c\bar{c}$ ) production cross section as a function of collision energy. Data points are from world-wide experimental measurements<sup>89–95</sup>. Theoretical calculations of next-to-leading-order (NLO) pQCD (MNR<sup>73</sup>) and their upper/lower limits are shown as black solid and dashed curves. The blue curve shows the result using the MNR line shape to fit world-wide data. Vertical bars around data points represent the total experimental uncertainties.



Extended Data Figure 3: Low mass excess dielectron invariant mass spectrum for Au+Au collisions at  $\sqrt{s_{NN}} = 27$  GeV (left) and 54.4 GeV (right), normalized by  $dN_{ch}/dy$ , compared to the theoretical calculations from the Rapp<sup>13,14,29,81</sup> and PHSD<sup>26,27</sup> models. Vertical bars and boxes around data points represent the statistical and systematic uncertainties, respectively.

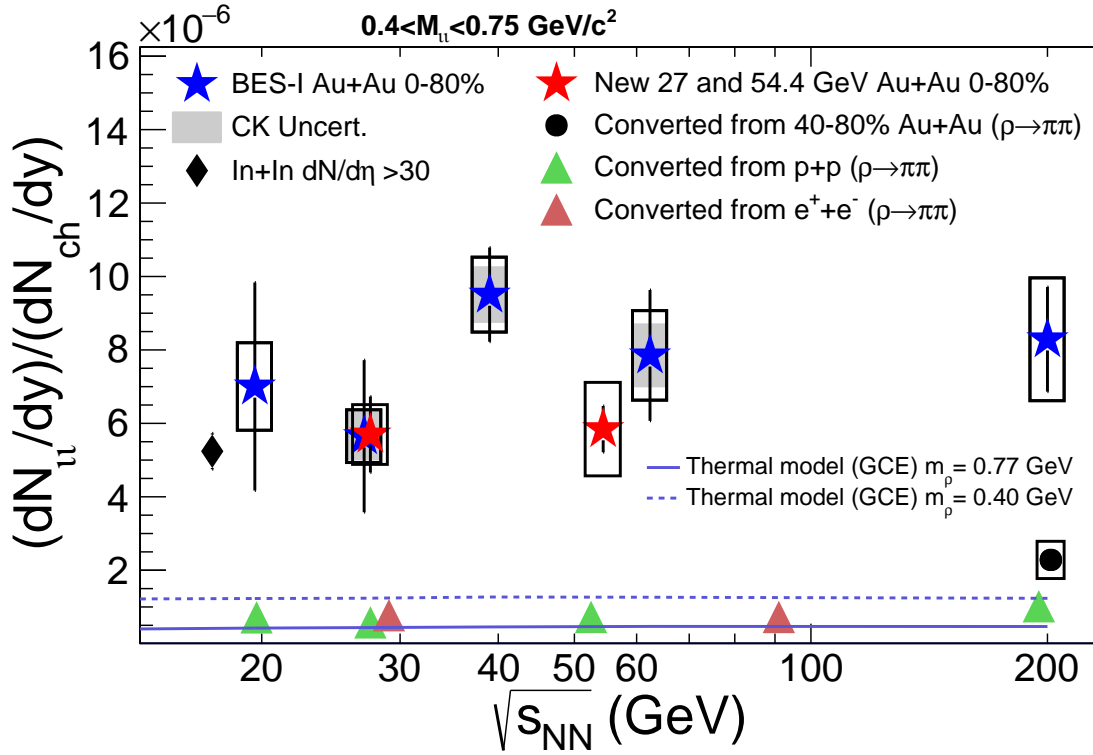


Extended Data Figure 4: Excess dielectron invariant mass spectrum for Au+Au collisions at  $\sqrt{s_{NN}} = 27$  GeV (left) and 54.4 GeV (right) in different centralities, compared to the theoretical calculations from the Rapp model (omitted in 54.4 GeV) <sup>13,14,29,81</sup> and the PHSD <sup>26,27</sup> model. Vertical bars and boxes around data points represent the statistical and systematic uncertainties, respectively.

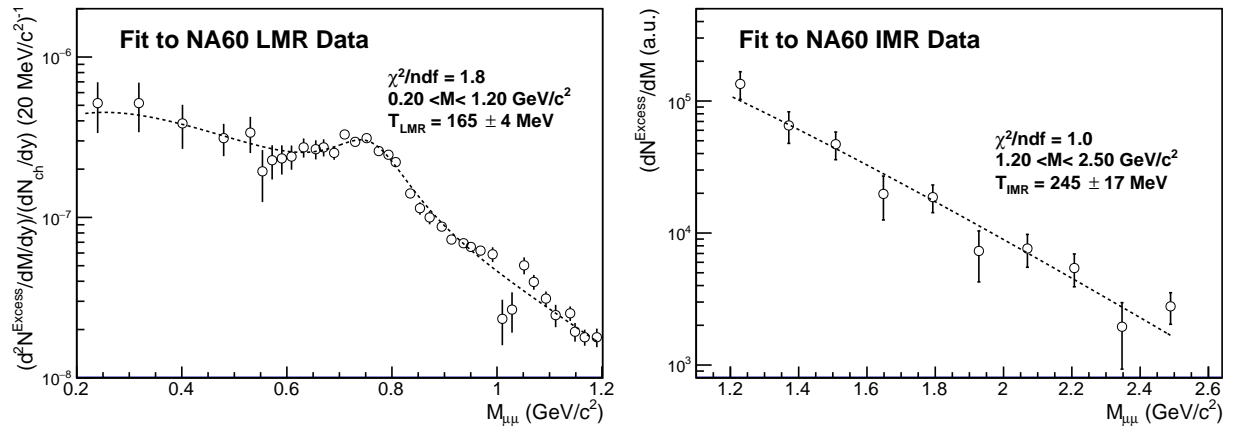


Extended Data Figure 5: Temperatures extracted from LMR and IMR as a function of the number of participating nucleons ( $N_{part}$ ) of  $\sqrt{s_{NN}} = 27$  GeV(left) and 54.4 GeV(right) Au+Au collisions. The dot-dash line shows the pseudo-critical temperature derived in LQCD calculations evaluated at  $\mu_B = 0$ . Vertical bars and shaded boxes around data points represent the statistical and systematic uncertainties, respectively.





Extended Data Figure 6: The collision-energy dependence of the integrated thermal dilepton yields in the mass range  $0.4 < M_{tt} < 0.75 \text{ GeV}/c^2$ , normalized by the charged particle density  $dN_{ch}/dy$ . Experimental data from this study and STAR BES-I data<sup>37,39</sup> are shown as red and blue stars, respectively. Triangles and the black circle represent the expected  $\rho \rightarrow e^+e^-$  result based on the  $\rho \rightarrow \pi^+\pi^-$  data measured in  $p+p$  collisions<sup>46,82-84</sup>,  $e^+ + e^-$  collisions<sup>47,85,86</sup> and Au+Au peripheral (40-80% centrality) collisions<sup>50</sup>. Vertical bars and open boxes around data points represent the statistical and systematic uncertainties, respectively. The solid and dashed lines show the theoretical prediction from the statistical thermal model (GCE) with chemical freeze-out parameters obtained by fitting to STAR measured hadrons<sup>52,96</sup>.



Extended Data Figure 7: The left panel shows temperature extraction from the NA60 published LMR thermal dimuon spectra <sup>34,87</sup>. The right panel shows temperature extraction from the NA60 published IMR thermal dimuon spectra <sup>35</sup>. Vertical bars in the left panel represent statistical uncertainty while vertical bars in the right panel denote the sum in quadrature of statistical and systematic uncertainties.